



Enhancing the open-circuit voltage in narrow-bandgap CuInSe₂ solar cells via local contact passivation with Al₂O₃

Dong-Hwan Jeon^{a,1}, Si-Nae Park^{b,1}, Jae-Baek Lee^a, Young-Ill Kim^a, Kee-Jeong Yang^a, Jin-Kyu Kang^a, Dae-Hwan Kim^a, Shi-Joon Sung^{a,**}, Dae-Kue Hwang^{a,*}

^a Daegu Gyeongbuk Institute of Science & Technology (DGIST), Research Center for Thin Film Solar Cells, Dalseong-gun, Daegu, 42988, South Korea

^b School of Electronic and Electrical Engineering, Kyungpook National University, 80 Daehak-ro, Daegu, 41566, South Korea

ARTICLE INFO

Keywords:

CISE
Narrow bandgap
Back contact
Passivation
Thin film solar cells

ABSTRACT

A fabrication technique using Al₂O₃-passivated local contacts was employed to produce narrow-bandgap CuInSe₂ (CISE) photoabsorbers, which are well-suited as bottom cell materials in tandem devices. However, the performances of CISE cells with narrow bandgaps are impeded by the recombination of charge carriers, which reduces the open-circuit voltage (V_{OC}). To overcome this limitation, an additional Al₂O₃ passivation layer was added to CISE solar cells. This enhanced the V_{OC} while maintaining a spectral response of up to 1.0 eV, thereby boosting the photovoltaic conversion efficiency of the devices. Further, the Al₂O₃ passivation layer within the CISE absorber effectively mitigated the recombination of charge carriers, resulting in a substantial improvement in efficiency. Specifically, the Al₂O₃-passivated local contact hindered the charge-carrier recombination at the rear contact, leading to a marked increase in the V_{OC} . Consequently, the overall photovoltaic conversion efficiency increased significantly from 10.4 % to 13 %. These results are expected to greatly further the development of CISE solar cells and achieve remarkable photovoltaic conversion efficiencies.

1. Introduction

Stacking solar cells with varying bandgap energies (E_g) to capture the entire solar light spectrum is a promising method for achieving efficiencies that surpass the Shockley–Queisser limit of approximately 30 % [1]. One particularly attractive approach involves integrating CuInGaSe (CIGS) solar cells as bottom cells in combination with perovskite solar cells because of their favorable attributes, including a high efficiency of 23.35 %, high radiation hardness, and long-term stability [2–6]. Furthermore, the bandgap of CIGS cells can be adjusted between 1.0 and 1.7 eV by varying the ratio of Ga to (Ga + In), allowing for the design of multijunction solar cells with appropriate E_g combinations [7]. In high-performance CIGS cells, the absorber layers often incorporate a graded Ga to (Ga + In) ratio across their thickness, which yields an intricate bandgap profile. Compositional grading in CIGS cells plays a vital role in reducing charge-carrier recombination at the rear contact, making it a pivotal factor in achieving high efficiency for CIGS cells [8,

9]. However, achieving compatibility between the bandgap values of the top and bottom cells is challenging; for example, the optimal bandgap for the bottom and top cells may be 0.94 and 1.60 eV, respectively [10]. This constraint necessitates a reduction in the bandgap of CuInSe₂ (~1.0 eV) in monolithic devices. Although there has been extensive research into CIGS cells with suitable bandgaps for single-junction cells, investigation on narrow-bandgap CISE cells without Ga has been relatively limited. While narrow-bandgap CISE cells have achieved a record efficiency of around 15.0 % [11–13], there is a significant gap between the theoretical maximum efficiency and the actual efficiency achieved with CISE cells, particularly with respect to the open-circuit voltage (V_{OC}).

Al₂O₃ has found widespread use as a passivation layer in Si photovoltaics and has been shown to improve Si solar cell performance in various studies [14,15]. Further, its application as a passivation layer on the back surface of CIGS cells has also shown positive outcomes [16–18]. Nonetheless, alternative materials have been investigated as passivation

Peer review under responsibility of Vietnam National University, Hanoi.

* Corresponding author.

** Corresponding author.

E-mail addresses: sjsung@dgist.ac.kr (S.-J. Sung), dkhwang@dgist.ac.kr (D.-K. Hwang).

¹ These authors contributed equally to this work.

<https://doi.org/10.1016/j.jسامd.2023.100648>

Received 23 August 2023; Received in revised form 6 November 2023; Accepted 8 November 2023

Available online 14 November 2023

2468-2179/© 2023 Vietnam National University, Hanoi. Published by Elsevier B.V. This is an open access article under the CC BY-NC-ND license (<http://creativecommons.org/licenses/by-nc-nd/4.0/>).

layers in other studies, including SiO₂ nanoparticles [19] or nanomeshes [20], MgF₂ layers [21], and TiO₂ layers [22], and have been prepared using diverse techniques. However, one limitation of using Al₂O₃ as a passivation layer is its role as an electron and diffusion barrier layer, which hinders current flow as well as sodium diffusion from the soda-lime glass substrate. We expected that the use of photolithography techniques to create contact openings in the layer would aid in overcoming this limitation; however, to date, contact openings in such passivation layers have rarely been reported.

In this study, for the first time, we attempted to improve the photovoltaic conversion efficiency (PCE) of CISE solar cells by adding a Al₂O₃ passivation layer. Through this approach, we achieved not only an improvement in the V_{OC} of CISE solar cells but also maintained the spectral response of the devices up to 1.0 eV. Further, the improved V_{OC} led to a corresponding enhancement in the PCE from 10.4 % to 13 %. In particular, we focused on the effects of Al₂O₃-passivated local contacts in the CISE absorber, which effectively reduced the recombination of charge carriers, thus enhancing the efficiency of CISE solar cells. Additionally, the Al₂O₃ passivation layer demonstrated a field passivation effect by introducing fixed negative charges and maintaining a low interface defect density. We expect that this step towards reducing carrier recombination will contribute to improving CISE solar cell efficiency.

2. Experimental

2.1. Al₂O₃ pattern preparation

Fig. 1 shows the fabrication process of the passivated solar cell. First, an 80-nm-thick Al₂O₃ thin-film was sputter-deposited onto the Mo substrate; the pressure of the sputtering chamber was set to 10⁻⁷ Torr prior to the Al₂O₃ thin film deposition, and the pressure was increased to 10 mTorr for the actual deposition by introducing a mixed gas of Ar (100 sccm) and O₂ (5 sccm) at a radiofrequency (RF) power of 500 W for a duration of 5000 s. The patterning of the 80-nm-thick Al₂O₃ thin-film involved five steps: (1) A positive photoresist was coated onto the

Al₂O₃-deposited substrate at 4000 rpm for 45 s (2) The solvent was then evaporated by soft baking the substrate at 130 °C for 60 s on a hot plate. (3) UV exposure using the i-line emission wavelength (365 nm) was performed under a constant intensity of 12 mW/cm² for 10 s (4) After UV exposure, the photoresist was developed for 45 s using an AZ-300 MIF developer to remove the unnecessary photoresist. (5) The Al₂O₃ thin film was then etched at a rate of 0.8 nm/s using the wet etching process with BOE 6:1, which is inexpensive and has a high etching rate. BOE 6:1 is six parts by volume 40 % ammonium fluoride and one part by volume 49 % hydrofluoric acid. Subsequently, the photoresist layer was removed using acetone. The dot pattern comprised an array of openings measuring 3–4 μm in diameter and separated by 8 μm; 80 % of the Mo back surface was covered by the passivating Al₂O₃ layer (Fig. 2(c) inset). The optimum thickness and dot size of Al₂O₃ were selected based on the CIGS solar cell, as shown in Figs. S1 and S2.

2.2 Device preparation.

2.3 Measurement of time-resolved photoluminescence.

2.4 Device measurement

Details can be found in [supporting information](#).

3. Results and discussion

The growth of the absorber on different substrates was investigated by X-ray diffractometry (XRD) and scanning electron microscopy (SEM). The growth direction of the CISE crystals on Mo was very similar to that of CISE (CISE 98-006-8334) crystals with the Al₂O₃-passivated local contact (Fig. 2(a)). Furthermore, the grain structure, size, and roughness of the CISE absorber layers were very similar to those of CISE with the Al₂O₃-passivated local contact (Fig. 2(b)). The different substrate configurations showed no significant differences in absorber grain size and morphology. However, the Mo peak intensity in the spectrum of the CISE sample deposited above Mo was higher than that in the spectrum of the sample deposited above Al₂O₃ as a result of the Al₂O₃ thin film; however, the CISE (112) and (220/024) peak intensities were similar, and no secondary peaks were observed. A cross-sectional transmission electron microscopy (TEM) image of the passivated solar cell (Fig. 2(c)) provides

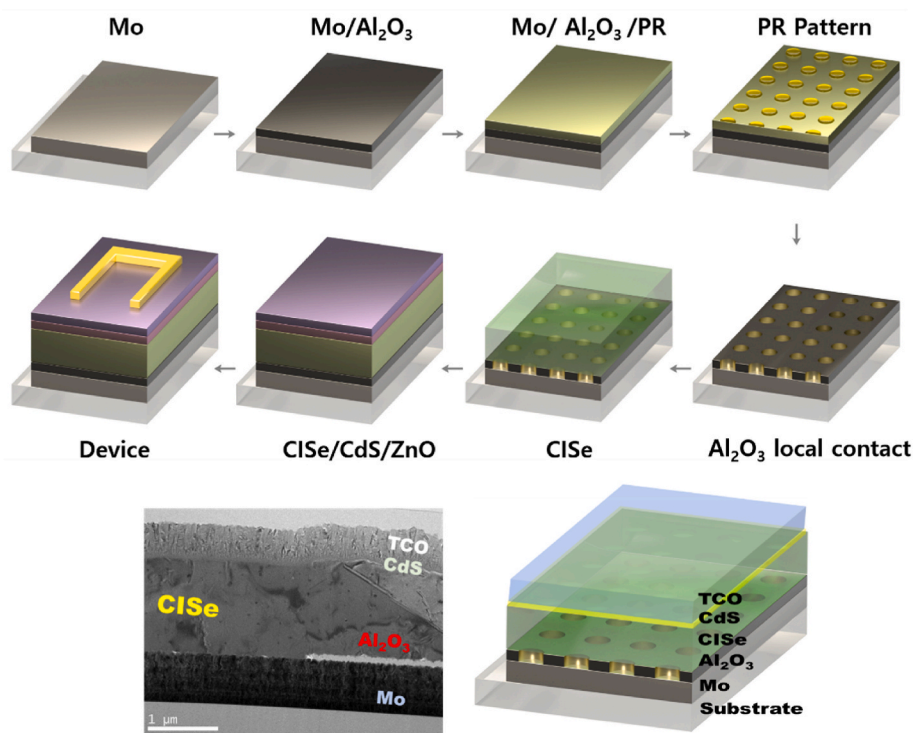


Fig. 1. Schematic of the fabrication process of a passivated CISE solar cell. The reference device does not include the Al₂O₃ deposition and patterning steps.

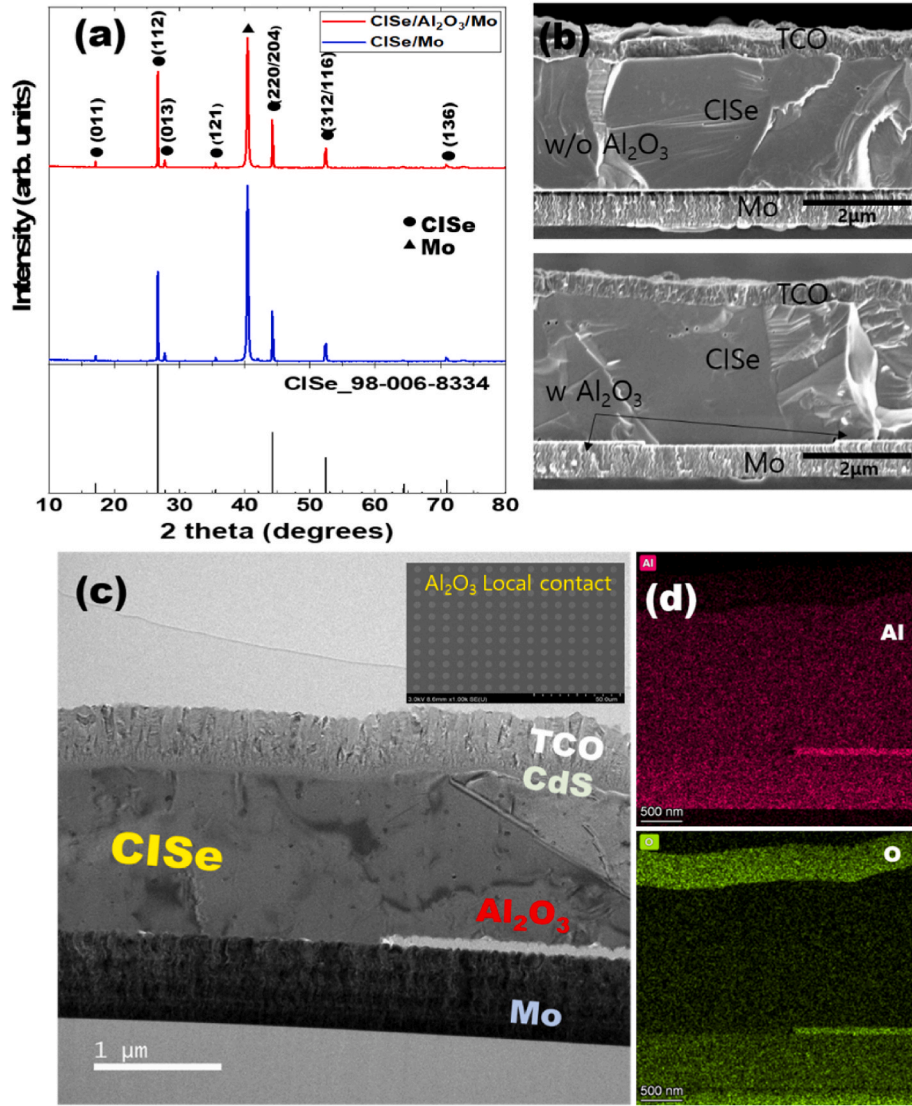


Fig. 2. (a) XRD patterns and (b) cross-sectional SEM images of CISE solar cells with different back contacts. (c) TEM image and (d) scanning TEM-energy-dispersive spectroscopy maps of Al and O for the passivated CISE solar cell with Al_2O_3 local contact.

a clear view of all solar cell layers, that is, Mo, Al_2O_3 , CISE, CdS, and ZnO. In the TEM image, the approximately 80-nm-thick Al_2O_3 passivation layer is prominently visible at the Mo/CISE interface, as revealed by the local contacts. The bright layer at the bottom of the image corresponds to the Al_2O_3 passivation layer, which exhibits patterned openings at its top. The 80-nm-thick Al_2O_3 layer contained specific openings known as point contacts, which were defined by the exposure and etching procedures. These point contacts formed circular pores with diameters of 4000 nm. The main function of these openings was to establish an electrical connection between the rear contact and the CISE absorbing layer by penetrating the electrically insulating Al_2O_3 layer. The TEM image emphasizes the durability of the Al_2O_3 layer with patterned contacts, showcasing its capacity to withstand the challenging CISE growth conditions, that is, 530 °C under a Se atmosphere. In addition, the elemental composition of the passivation layer was confirmed using TEM and energy dispersive X-ray spectroscopy (EDS) (Fig. 2(d)), which also demonstrated that the interface between Al_2O_3 and CISE was clearly maintained. Additionally, depth profile secondary-ion mass spectrometry (SIMS) was conducted; the data for Al is shown in Fig. S3.

Table 1 summarizes the differences in the performance of CISE cells with and without the Al_2O_3 -passivated local contact. An evident

Table 1

Photovoltaic performance parameters of CISE solar cells with different back contacts.

| | J_{SC} [mA/cm ²] | V_{OC} [V] | Fill factor (FF) [%] | PCE [%] | E_g [V] | V_{OC} deficit [V] |
|----------------------------------|--------------------------------|--------------|----------------------|---------|-----------|----------------------|
| CISE | 38.1 | 0.40 | 69.1 | 10.4 | 0.99 | 0.59 |
| CISE w./ Al_2O_3 | 38.2 | 0.47 | 73.1 | 13.0 | 0.99 | 0.52 |

improvement in V_{OC} was observed upon local contact passivation with Al_2O_3 . The deficit calculated from E_g and the electrical gain (V_{OC}) (Table 1) can be used to calculate the effect of the Al_2O_3 -passivated local contact on V_{OC} . The E_g value was determined by linearly extrapolating a plot of (photon energy \times external quantum efficiency (EQE))² against photon energy, as shown in Fig. S4. Upon implementing the Al_2O_3 -passivated local contact, there was an approximate increase of 70 mV in the V_{OC} . In Fig. 3(a), a comparison of the current–voltage (J–V) curves is shown for two solar cells with similar bandgaps but differing Al_2O_3 -passivated local contacts. The solar cell incorporating the Al_2O_3 -passivated local contact demonstrated a significantly higher V_{OC} , which can be attributed to an effective reduction in charge-carrier

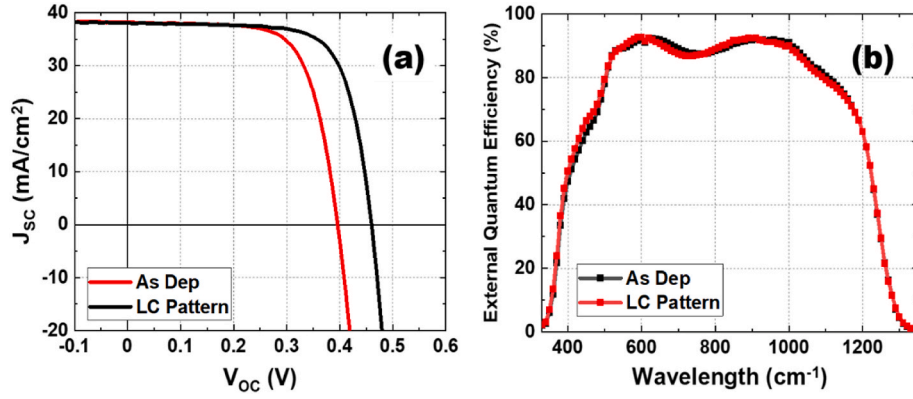


Fig. 3. (a) J–V characteristics and (b) EQE spectra of CISE solar cells with different back contacts.

recombination at the back contact. In addition, the PCE increased from 10.4 % to 13 % owing to the increased V_{OC} . Meanwhile, although the CISE solar cell with the Al_2O_3 passivation layer exhibited a slightly higher short-circuit current (J_{SC}) than that without, the J_{SC} values of both solar cells were comparable because the cells had the same bandgap, as shown in Fig. S4 [23].

To provide further evidence for the improvement in V_{OC} attributable to the Al_2O_3 -passivated local contact, time-resolved photoluminescence (TRPL) measurements were conducted; TRPL decay analysis provides valuable insights into carrier dynamics within absorbers, and this information is linked to material properties, which then allows us to establish a relationship between the TRPL lifetime and the Al_2O_3 -passivated local contact [23–25]. TRPL measurements were conducted on selected absorbers with different Al_2O_3 -passivated local contacts; the measurements were performed without a CdS buffer layer (Fig. 4). To account for the influence of the distribution of recombination rate constants on the decay kinetics, we calculated the emission lifetimes using triexponential decay kinetics [26–28]. Table 2 shows the relevant parameters and corresponding values. The average carrier lifetime (τ_{avg}) was then determined using Equation (1) [26,29]:

$$\tau_{avg} = (\tau_1^2 A_1 + \tau_2^2 A_2 + \tau_3^2 A_3) / (\tau_1 A_1 + \tau_2 A_2 + \tau_3 A_3) \quad (1)$$

where A_1 , A_2 , and A_3 represent the relative amplitudes of the carrier lifetimes, and τ_1 , τ_2 , and τ_3 are the respective fluorescence lifetimes. The average time constant (τ_{avg}) provides valuable insights into the decay dynamics of excited-state- and free-carrier recombination in CISE layers.

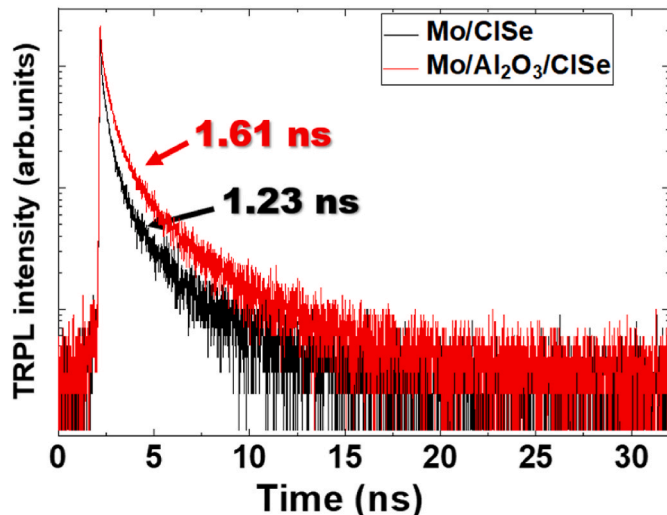


Fig. 4. TRPL transients of CISE absorbers with different back contacts.

Table 2

TRPL parameters of CISE absorbers with different back contacts obtained by fitting the TRPL spectra.

| | τ_1 [ns] | A_1 [ns] | τ_2 [ns] | A_2 [ns] | τ_3 [ns] | A_3 [ns] | τ_{ave} [ns] |
|-----------------------|------------------|---------------|------------------|---------------|------------------|---------------|----------------------|
| CISE | 2.800 | 0.074 | 0.43 | 0.74 | 0.057 | 0.990 | 1.23 |
| CISE w./ Al_2O_3 | 0.566 | 0.980 | 3.20 | 0.136 | 0.09 | 0.953 | 1.61 |

The CISE with Al_2O_3 -passivated local contacts was found to have a higher τ_{avg} (1.61 ns) than that without (1.23 ns). This implies that photogenerated carriers had a longer lifetime, allowing for increased transfer and collection by the n-type layer. Therefore, the use of Al_2O_3 -passivated local contacts effectively inhibited charge-carrier recombination at the rear contact, resulting in a longer carrier lifetime.

Per the literature, τ_1 and τ_2 are associated with the fast-decay component, attributed to bulk recombination in CISE, whereas τ_3 corresponds to the slow-decay component resulting from the recombination of free carriers in the radiative channels [30]. To examine the influence of the Al_2O_3 passivation layer, CISE absorbers were mechanically delaminated from the Mo rear contact using transparent epoxy glue, following a literature procedure [23]. Two sets of samples were prepared—one with the Al_2O_3 passivation layer and the other without. Both absorbers showed longer lifetimes after delamination of the Al_2O_3 passivation layer because of the CISE/air interface, which has a lower back surface recombination velocity than the CISE/Mo contact [23,31]. Furthermore, the delamination resulted in both samples exhibiting almost the same lifetime, as shown in Table S1. The experimental results rule out the possibility of the improved V_{OC} arising from variations in absorber doping concentration or bandgap, as both were found to be similar (Fig. S4). Thus, it was confirmed that the Al_2O_3 passivation layer modified the density of back surface defects, influencing the generated charge carriers [32–34].

Next, we used C–V measurements to gain fundamental insights into the device properties, allowing the evaluation of the charge density. The charge density (N_a) and built-in voltage at the cell junction were determined from a plot of $1/C^2$ against V , based on Equations (2) and (3) [35,36]:

$$\frac{1}{C^2} = \frac{2}{qN_a \epsilon_0 \epsilon_s A^2} (V_{bi} - V) \quad (2)$$

$$N_a = \frac{2}{q \epsilon_0 \epsilon_s A^2 \left[\frac{d}{dV} \left(\frac{1}{C^2} \right) \right]} \quad (3)$$

where N_a is the charge density ($1/cm^3$), q is the electron charge (1.60219×10^{-19} C), ϵ_0 is the permittivity of free space (8.85×10^{-14} F/

cm), ϵ_s is the dielectric constant of ClSe (13.4), A is the area of the cell (0.185 cm^2), C is the measured capacitance, and V is the applied direct current (DC) voltage. Using Equations (2) and (3), the built-in-potential (V_{bi}) and doping density can be obtained from the intercept and slope of the line $1/C^2$ against V . Furthermore, using Equation (3), the charge densities (N_a) of the reference and passivated devices were calculated to be 7.9×10^{16} and $5.7 \times 10^{16} \text{ cm}^{-3}$, respectively.

To calculate the V_{OC} , we employed Equation (4) [37], where K_B , T , and q represent the Boltzmann's constant, temperature, and elemental charge, respectively. According to the equation, increasing the carrier concentration should result in a higher V_{OC} . To investigate the role of carrier concentration in determining the V_{OC} , we conducted capacitance–voltage (C–V) measurements to determine the charge densities $N_{a, \text{ref}}$ and $N_{a, \text{pass}}$, and then calculated the contribution of the variation in N_a (ΔV) to the V_{OC} of cells having different back contacts.

$$\Delta V_{OC} = \frac{K_B T}{q} \ln \left(\frac{N_{a, \text{ref}}}{N_{a, \text{pass}}} \right) \quad (4)$$

Because the Al_2O_3 layer is known to inhibit sodium diffusion, we also extracted carrier concentration values from the C–V measurements to evaluate the effect of the Al_2O_3 layer on the sodium concentration. Our findings revealed that the carrier concentration of the reference cell was marginally higher compared to that of the passivated cell, indicating that it contained a relatively higher sodium concentration than the passivated cell. Williams et al. reported that introducing sodium using NaF precursor layers with different thicknesses increased the V_{OC} and carrier concentration by approximately 1 mV and $1 \times 10^{16} \text{ cm}^{-3}$, respectively [38]. In our study, we observed a difference in carrier concentration of $2.2 \times 10^{16} \text{ cm}^{-3}$ between reference ($7.9 \times 10^{16} \text{ cm}^{-3}$) and passivated ($5.7 \times 10^{16} \text{ cm}^{-3}$) devices. We also measured the hole concentration of the ClSe film of reference ($1.7 \times 10^{16} \text{ cm}^{-3}$) and passivated ($1.4 \times 10^{16} \text{ cm}^{-3}$) devices using Hall measurements and found that the charge densities obtained in the C–V measurements were higher than those obtained in the Hall measurements, likely because of the inclusion of the interfacial charge density in the C–V measurements. However, both the C–V and Hall measurements showed that the reference device had a higher carrier concentration than the passivated device. Even with this carrier concentration difference, the expected difference in V_{OC} between the reference and passivated solar cells was only ~ 2 mV, which is much smaller than the observed improvement in V_{OC} . Therefore, we concluded that the observed improvement in V_{OC} that arose from the Al_2O_3 -passivation local contact could not be attributed to variations in carrier concentration or sodium concentration. Instead, we attribute this effect to the inhibition of the recombination of charge carriers at the back surface. To verify the differences in parameters between the reference ClSe solar cell device and the device with passivation, all experimental results for both devices were plotted together in a single graph (Fig. 5). The improvement in the V_{OC} of the ClSe sample deposited on the Al_2O_3 local contact was remarkable. Band alignment of the Al_2O_3 passivation layer and absorber layer was also calculated using SCACE-1D (Fig. S5). These results confirm that the ClSe device deposited on the Al_2O_3 local contact was affected by passivation.

4. Conclusion

In this study, we investigated the influence of an Al_2O_3 local contact passivation layer on the V_{OC} of narrow-bandgap ClSe solar cells. By comparing ClSe solar cells with and without the Al_2O_3 passivation layer, we observed that the addition of a passivation layer with point-contact openings significantly reduced charge-carrier recombination at the rear contact, resulting in a substantial increase in V_{OC} . Consequently, the PCE of the ClSe solar cells improved from 10.4 % to 13 %. Furthermore, the spectral response of the devices was preserved up to 1.0 eV. These ClSe solar cells are, therefore, highly suitable as bottom cells in monolithic thin film tandem devices as they can enable efficient current-matching

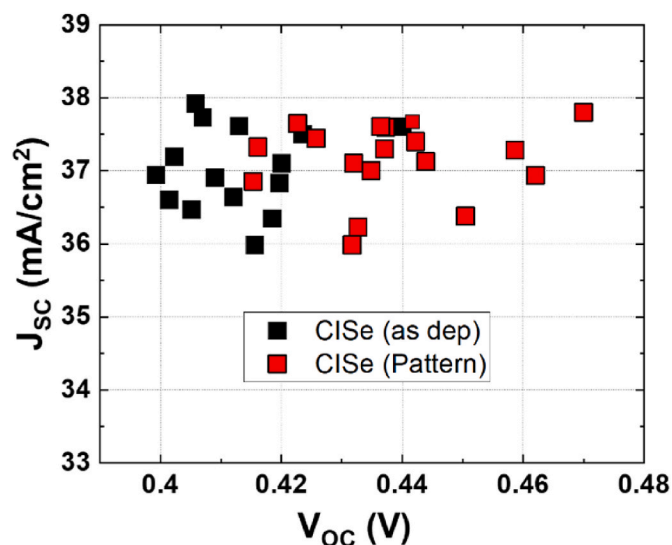


Fig. 5. Effect of Al_2O_3 passivation layer on the (a) short-circuit current density and (b) open-circuit voltage of ClSe solar cells.

with top cells equipped with wide-bandgap absorbers, such as halide-based perovskite devices. Although perovskite solar cells may have lower stability and durability compared to chalcopyrite solar cells, they offer advantages such as high efficiencies with large bandgaps and the potential for low-temperature fabrication processes. Therefore, the combination of ClSe solar cells with perovskite top cells holds promise for achieving efficient and stable tandem solar devices. Hence, current research is focused on using perovskite solar cells as upper solar cells in combination with Si, ClGSe, and ClSe bottom solar cells.

Data availability

Data will be made available upon request with proper justification.

Declaration of competing interest

The authors declare that they have no known competing financial interests or personal relationships that could have appeared to influence the work reported in this paper.

Acknowledgements

This work was supported in part by the program of Phased development of carbon neutral technologies (2022M3J1A1085371) through NRF (National Research Foundation of Korea) and in part by DGSIT R&D Program of the Ministry of Science and ICT of Korea (Grant numbers 23-ET-08 and 23-CoE-ET-01).

Appendix A. Supplementary data

Supplementary data to this article can be found online at <https://doi.org/10.1016/j.jsamd.2023.100648>.

References

- [1] B. Ehrler, E. Alarcón-Lladó, S.W. Tabernig, T. Veeken, E.C. Garnett, A. Polman, Photovoltaics reaching for the Shockley–Queisser limit, *ACS Energy Lett.* 5 (2020) 3029–3033, <https://doi.org/10.1021/acsenenergylett.0c01790>.
- [2] M.A. Ruiz-Preciado, F. Gota, P. Fassi, I.M. Hossain, R. Singh, F. Laufer, F. Schackmar, T. Feeney, A. Farag, I. Allegro, H. Hu, S. Gharibzadeh, B.A. Nejjad, V.S. Gevaerts, M. Simor, P.J. Bolt, U.W. Paetzold, Monolithic two-terminal perovskite/CIS tandem solar cells with efficiency approaching 25%, *ACS Energy Lett.* 7 (2022) 2273–2281, <https://doi.org/10.1021/acsenenergylett.2c00707>.
- [3] D.H. Jeon, S.Y. Kim, T. Enkhbat, J.H. Kim, D.H. Kim, D.K. Hwang, Improvement of Ga distribution with Sb incorporation for two-step low-temperature processing of

- CIGSe thin film solar cells, *Sol. Energy Mater. Sol. Cells* 194 (2019) 244–251, <https://doi.org/10.1016/j.solmat.2019.02.024>.
- [4] K.J. Yang, J.H. Sim, D.H. Son, D.H. Jeon, D.K. Hwang, D. Nam, H. Cheong, S. Y. Kim, J.H. Kim, D.H. Kim, J.K. Kang, Comparison of chalcopyrite and kesterite thin-film solar cells, *J. Ind. Eng. Chem.* 45 (2017) 78–84, <https://doi.org/10.1016/j.jiec.2016.09.005>.
 - [5] B.S. Ko, S.J. Sung, D.H. Kim, D.H. Lee, D.K. Hwang, Effects of annealing on structural and electrical properties of sub-micron thick CIGS films, *Curr. Appl. Phys.* 13 (2013) S135–S139, <https://doi.org/10.1016/j.cap.2013.01.022>.
 - [6] B.S. Ko, S.J. Sung, D.K. Hwang, Characterization of in-situ annealed sub-micron thick Cu(In,Ga)Se₂ thin films, *Thin Solid Films* 590 (2015) 330–334, <https://doi.org/10.1016/j.tsf.2015.02.053>.
 - [7] H.J. Jo, D.H. Kim, C. Kim, D.K. Hwang, S.J. Sung, J.H. Kim, I.H. Bae, The optical and structural properties of CuIn_{1-x}Ga_xSe₂ thin films fabricated with various Ga contents by using the co-evaporation technique, *J. Kor. Phys. Soc.* 60 (2012) 1708–1712, <https://doi.org/10.3938/jkps.60.1708>.
 - [8] D.K. Hwang, B.S. Ko, D.H. Jeon, J.K. Kang, S.J. Sung, K.J. Yang, D. Nam, S. Cho, H. Cheong, D.H. Kim, Single-step sulfo-selenization method for achieving low open circuit voltage deficit with band gap front-graded Cu₂ZnSn(S,Se)₄ thin films, *Sol. Energy Mater. Sol. Cells* 161 (2017) 162–169, <https://doi.org/10.1016/j.solmat.2016.11.034>.
 - [9] A.F. Violas, A.J.N. Oliveira, J.P. Teixeira, T.S. Lopes, J.R.S. Barbosa, P. A. Fernandes, P.M.P. Salomé, Will ultrathin CIGS solar cells overtake the champion thin-film cells? Updated SCAPS baseline models reveal main differences between ultrathin and standard CIGS, *Sol. Energy Mater. Sol. Cells* 243 (2022), 111792, <https://doi.org/10.1016/j.solmat.2022.111792>.
 - [10] M. Jöst, T. Bertram, D. Koushik, J.A. Marquez, M.A. Verheijen, M.D. Heinemann, E. Köhnen, A. Al-Ashouri, S. Braunger, F. Lang, B. Rech, T. Unold, M. Creatore, I. Lauermann, C.A. Kaufmann, R. Schlattmann, S. Albrecht, 21.6%-Efficient monolithic perovskite/Cu(In,Ga)Se₂ tandem solar cells with thin conformal hole transport layers for integration on rough bottom cell surfaces, *ACS Energy Lett.* 4 (2019) 583–590, <https://doi.org/10.1021/acsenenergylett.9b00135>.
 - [11] S.H. Moustafa, H.M. Taha, S. Abdel-Samad, Studying the optical and electrical properties of CuGa_{0.5}In_{0.5}Se₂ chalcopyrite due to substrate temperature and gamma irradiation, *Phys. Status Solidi B Basic Res.* 259 (2022), 2100396, <https://doi.org/10.1002/pssb.202100396>.
 - [12] S. Suresh, D.J. Rokke, A.A. Drew, E. Alruqobah, R. Agrawal, A.R. Uhl, Extrinsic doping of ink-based Cu(In,Ga)(S,Se)₂ absorbers for photovoltaic applications, *Adv. Energy Mater.* 12 (2022), 2103961, <https://doi.org/10.1002/aenm.202103961>.
 - [13] Z. Wu, E. Bi, L.K. Ono, D. Li, O.M. Bakr, Y. Yan, Y. Qi, Passivation strategies for enhancing device performance of perovskite solar cells, *Nano Energy* 115 (2023), 108731, <https://doi.org/10.1016/j.nanoen.2023.108731>.
 - [14] D. Suh, Status of Al₂O₃/TiO₂-based antireflection and surface passivation for silicon solar cells, *Phys. Status Solidi Rapid Res. Lett.* 15 (2021), 2100236, <https://doi.org/10.1002/pssr.202100236>.
 - [15] X. Wang, G. Zhang, B. Liu, Y. Wang, C. Zhao, C. Pei, H. Deng, W. Han, T. Wang, J. Gong, Scaling-up of thin-film photoelectrodes for solar water splitting based on atomic layer deposition, *ACS Appl. Mater. Interfaces* 15 (2022) 1138–1147, <https://doi.org/10.1021/acsmi.2c18480>.
 - [16] D. Kim, S.S. Shin, Y. Jo, S.M. Lee, S.K. Ahn, J.S. Cho, J.H. Yun, H.S. Lee, J.H. Park, Practical enhancements in current density and power generation of bifacial semitransparent ultrathin CIGSe solar cells via utilization of wide bandgap zn-based buffer, *Adv. Sci.* 9 (2022), e2105436, <https://doi.org/10.1002/advs.202105436>.
 - [17] X. Chang, J. Chen, S. Ma, B. Chen, X. Zhang, Q. Gao, F. Li, J. Wang, D. Song, J. Chen, Implementation of tunneling junction passivated contact concept in flexible CIGS solar cells, *Adv. Mater. Interfac.* 10 (2023), 2202171, <https://doi.org/10.1002/admi.202202171>.
 - [18] J. de Wild, R. Scaffidi, G. Brammertz, G. Birant, B. Vermang, Dielectric front passivation for Cu(In,Ga)Se₂ solar cells: status and prospect, *Adv. Energy Sustain. Res.* 4 (2023), 2200132, <https://doi.org/10.1002/aesr.202200132>.
 - [19] G.S. Park, S.J. Lee, D.S. Kim, S.Y. Park, J.H. Koh, D.H. Won, P. Lee, Y.R. Do, B. K. Min, Amorphous TiO₂ passivating contacts for Cu(In,Ga)(S,Se)₂ ultrathin solar cells: defect-state-mediated hole conduction, *Adv. Energy Mater.* 13 (2023), 2203183, <https://doi.org/10.1002/aenm.202203183>.
 - [20] Y. Li, G. Yin, Y. Tu, S. Sedaghat, Y. Gao, M. Schmid, Ultrathin Cu(In,Ga)Se₂ solar cells with a passivated back interface: a comparative study between Mo and In₂O₃: Sn back contacts, *ACS Appl. Energy Mater.* 5 (2022) 7956–7964, <https://doi.org/10.1021/acsaem.2c00088>.
 - [21] B.F. Gonçalves, S. Sadewasser, L.M. Salonen, S. Lanceros-Méndez, Y.V. Kolen'ko, Merging solution processing and printing for sustainable fabrication of Cu(In,Ga)Se₂ photovoltaics, *Chem. Eng. J.* 442 (2022), 136188, <https://doi.org/10.1016/j.cej.2022.136188>.
 - [22] P. Anacleto, C. Hägglund, W.C. Chen, M. Kovačič, J. Krč, M. Edoff, S. Sadewasser, Precisely nanostructured HfO₂ rear passivation layers for ultra-thin Cu(In,Ga)Se₂, *Prog. Photovoltaics Res. Appl.* 30 (2022) 1289–1297, <https://doi.org/10.1002/ppp.3576>.
 - [23] W. Wang, S. Wang, Z. Chi, J. Luo, H. Yan, J. Gong, J. Li, X. Xiao, Surface engineering of submicron Cu(In,Ga)Se₂ for high-efficient Zn(O,S)-based solar cells with lower light soaking effects, *ACS Appl. Energy Mater.* 6 (2023) 2151–2159, <https://doi.org/10.1021/acsaem.2c02978>.
 - [24] K. Oliveira, J.P. Teixeira, W.C. Chen, J. Lontchi Jiole, A.J.N. Oliveira, I. Caha, L. D. Francis, D. Flandre, M. Edoff, P.A. Fernandes, P.M.P. Salomé, SiO_x patterned based substrates implemented in Cu(In,Ga)Se₂ ultrathin solar cells: optimum thickness, *IEEE J. Photovoltaics* 12 (2022) 954–961, <https://doi.org/10.1109/JPHOTOV.2022.3165764>.
 - [25] M. Ochoa, S.C. Yang, S. Nishiwaki, A.N. Tiwari, R. Carron, Charge carrier lifetime fluctuations and performance evaluation of Cu(In,Ga)Se₂ absorbers via time-resolved-photoluminescence Microscopy, *Adv. Energy Mater.* 12 (2022), 2102800, <https://doi.org/10.1002/aenm.202102800>.
 - [26] D.K. Hwang, H.J. Jo, D.H. Kim, E.J. Lee, R.P.H. Chang, Hybrid dual-stage flow-synthesis of eco-friendly ZnCuInS₂ quantum dots for solar cells: improvement in efficiency using inorganic ligand exchange, *J. Power Sources* 555 (2023), 232344, <https://doi.org/10.1016/j.jpowsour.2022.232344>.
 - [27] L. Liang, H. Zhang, T. Li, W. Li, J. Gao, H. Zhang, M. Guo, S. Gao, Z. He, F. Liu, C. Ning, H. Cao, G. Yuan, C. Liu, Addressing the conflict between mobility and stability in oxide thin-film transistors, *Adv. Sci.* 10 (2023), e2300373, <https://doi.org/10.1002/advs.202300373>.
 - [28] S. Yin, Y. Han, T. Yan, Q. Fu, T. Xu, W. Wu, Ultrafast carrier dynamics in SnSe thin film studied by femtosecond transient absorption technique, *Phys. B Condens. Matter* 622 (2021), 413347, <https://doi.org/10.1016/j.physb.2021.413347>.
 - [29] M. Jerigova, Y. Markushyna, I.F. Teixeira, B. Badamdorj, M. Isaacs, D. Cruz, I. Lauermann, M.Á. Muñoz-Márquez, N.V. Tarakina, N. López-Salas, O. Savateev, P. Jimenez-Calvo, Green light photoelectrocatalysis with sulfur-doped carbon nitride: using triazole-purpald for enhanced benzylamine oxidation and oxygen evolution reactions, *Adv. Sci.* 10 (2023), e2300099, <https://doi.org/10.1002/advs.202300099>.
 - [30] P. Qin, J. Zhang, G. Yang, X. Yu, G. Li, Potassium-intercalated rubrene as a dual-functional passivation agent for high efficiency perovskite solar cells, *J. Mater. Chem. A* 7 (2019) 1824–1834, <https://doi.org/10.1039/c8ta09026b>.
 - [31] S. Siebentritt, T.P. Weiss, M. Sood, M.H. Wolter, A. Lomuscio, O. Ramirez, How photoluminescence can predict the efficiency of solar cells, *J. Phys. Mater.* 4 (2021), 42010, <https://doi.org/10.1088/2515-7639/ac266e>.
 - [32] B. Li, X. Tan, J. Zhao, X. Han, Experimental and modeling analysis of photocarrier dynamics in CZTSSe using temperature-dependent photoluminescence, *Mater. Sci. Eng. B Solid-State Mater. Adv. Technol.* 284 (2022), 115897, <https://doi.org/10.1016/j.mseb.2022.115897>.
 - [33] A. Lafuente-Sampietro, K. Yoshida, S. Wang, S. Ishizuka, H. Shibata, N. Sano, K. Akimoto, T. Sakurai, Effect of the double grading on the internal electric field and on the carrier collection in CIGS solar cells, *Sol. Energy Mater. Sol. Cells* 223 (2021), 110948, <https://doi.org/10.1016/j.solmat.2020.110948>.
 - [34] T. Nishimura, J. Chantana, A. Mavlonov, Y. Kawano, T. Masuda, T. Minemoto, Device design for high-performance bifacial Cu(In,Ga)Se₂ solar cells under front and rear illuminations, *Sol. Energy* 218 (2021) 76–84, <https://doi.org/10.1016/j.solener.2021.01.075>.
 - [35] A. Ait Abdelkadir, M. Sahal, Theoretical development of the CZTS thin-film solar cell by SCAPS-1D software based on experimental work, *Mater. Sci. Eng. B* 296 (2023), 116710, <https://doi.org/10.1016/j.mseb.2023.116710>.
 - [36] J.O. Bodunrin, D.A. Oeba, S.J. Moloi, Current-voltage and capacitance-voltage characteristics of cadmium-doped p-silicon Schottky diodes, *Sens. Actuators A Phys.* 331 (2021), 112957, <https://doi.org/10.1016/j.sna.2021.112957>.
 - [37] R. Kumari, M. Mamta, R. Kumar, Y. Singh, V.N. Singh, 24% Efficient, simple ZnSe/Sb₂Se₃ heterojunction solar cell: an analysis of PV characteristics and defects, *ACS Omega* 8 (2022) 1632–1642, <https://doi.org/10.1021/acsomega.2c07211>.
 - [38] S. Giraldo, M. Neuschitzer, M. Placidi, P. Pistor, A. Perez-Rodriguez, E. Saucedo, Cu₂ZnSnSe₄-based solar cells with efficiency exceeding 10% by adding a superficial Ge nanolayer: the interaction between Ge and Na, *IEEE J. Photovoltaics* 6 (2016) 754–759, <https://doi.org/10.1109/JPHOTOV.2016.2535236>.